

1 **Towards an improved representation of carbonaceous aerosols over the**
2 **Indian monsoon region in a regional climate model RegCM**

3

4 Sudipta Ghosh¹, *Sagnik Dey^{1,2}, Sushant Das³, Nicole Riemer⁴, Graziano Giuliani³, Dilip
5 Ganguly¹, Chandra Venkatraman⁵, Filippo Giorgi³, Sachchida Nand Tripathi⁶, Ramachandran
6 Srikanthan⁷, Rajesh Ayyappan Thazhathakal⁷, Harish Gadhavi⁷, Atul Kumar Srivastava⁸

7

8 ¹Centre for Atmospheric Sciences, Indian Institute of Technology Delhi, India

9 ²Centre of Excellence for Research on Clean Air, Indian Institute of Technology Delhi, India

10 ³Earth System Physics Section, ICTP, Trieste, Italy

11 ⁴Department of Atmospheric Sciences, University of Illinois at Urbana-Champaign, IL, USA

12 ⁵Department of Chemical Engineering, Indian Institute of Technology Bombay, India

13 ⁶Department of Civil Engineering, Indian Institute of Technology Kanpur, India

14 ⁷Space and Atmospheric Sciences Division, Physical Research Laboratory, Ahmedabad, India

15 ⁸Indian Institute of Tropical Meteorology, New Delhi Branch, India

16

17 ***Correspondence:** sagnik@cas.iitd.ac.in

18

19 **Keywords:** RegCM4; emission inventory; carbonaceous aerosols; model customization;
20 Indian monsoon region

21

22 **Abstract.** Mitigation of carbonaceous aerosol emissions is expected to provide climate and
23 health co-benefits. The accurate representation of carbonaceous aerosols in climate models is
24 critical for reducing uncertainties in their climate feedback. In this regard, emission fluxes and
25 aerosol life-cycle processes are the two primary sources of uncertainties. Here we demonstrate
26 that incorporating a dynamic ageing scheme and emission estimates that are updated for the
27 local sources improve the representation of carbonaceous aerosols over the Indian monsoon
28 region in a regional climate model, RegCM, compared to its default configuration. The mean
29 BC and OC surface concentrations in 2010 are estimated to be 4.25 and 10.35 $\mu\text{g m}^{-3}$,
30 respectively, over the Indo-Gangetic Plain (IGP), in the augmented model. The BC column
31 burden over the polluted IGP is found to be 2.47 mg m^{-2} , 69.95 % higher than in the default
32 model configuration and much closer to available observations. The anthropogenic AOD
33 increases by more than 19 % over the IGP due to the model enhancement, also leading to a

34 better agreement with observed AOD. The top-of-the-atmosphere, surface, and atmospheric
35 anthropogenic aerosol shortwave radiative forcing are estimated at -0.3, -9.3, and 9.0 W m^{-2} ,
36 respectively, over the IGP and -0.89, -5.33, and 4.44 W m^{-2} , respectively, over Peninsular India
37 (PI). Our results suggest that both accurate estimates of emission fluxes and a better
38 representation of aerosol processes are required to improve the aerosol life cycle representation
39 in the climate model.

40

41 **1. Introduction**

42 Carbonaceous aerosols (organic carbon, OC, and black carbon, BC) emitted from
43 incomplete combustion constitute 20%-50% of the total global aerosol mass (Kanakidou et al.,
44 2005; Putaud et al., 2010), causing substantial air quality degradation (Singh et al., 2021). Due
45 to their ability to absorb solar radiation, carbonaceous aerosols also contribute to global
46 warming (Ramanathan and Carmichael, 2008). Hence, they are considered to be key short-
47 lived climate pollutants (SLCPs) (UNFCCC, 2015), and mitigating their emissions is expected
48 to result in both climate and health co-benefits (Tibrewal and Venkataraman, 2021; Naik et al.,
49 2021). Climate models are characterized by large discrepancies in simulating carbonaceous
50 aerosol loadings, their optical properties, and radiative forcing (Ajay et al., 2019), primarily
51 due to uncertainties in emission inventories and limitations in the treatment of aerosol processes
52 in the models (Bond et al., 2013). Unless the representation of the life cycle of carbonaceous
53 aerosols in climate models is improved, their role in climate impacts and air quality degradation
54 cannot be assessed accurately (Riemer et al., 2019).

55 A multi-institutional network program - Carbonaceous aerosol emissions, source
56 apportionment, and climate impacts (COALESCE) was launched by the Government of India
57 to address some of these issues for the Indian monsoon region (Venkataraman et al., 2020).
58 One of the scientific objectives of COALESCE is to understand and reduce uncertainties in
59 representing carbonaceous aerosol life cycle in global and regional climate models, focusing
60 on the Indian subcontinent. The regional climate model, RegCM4, developed at the
61 International Centre for Theoretical Physics (ICTP), Italy (Giorgi et al., 2012), is one of the
62 participating models in COALESCE. RegCM4 was extensively used to examine variability in
63 the Indian summer monsoon (Dash et al., 2015; Rai et al., 2020), to project climate change over
64 South Asia (Pattnayak et al., 2018), and to elucidate the dynamical impacts of aerosols on the
65 Indian summer monsoon in the present (Das et al., 2015, 2016) and future (Das et al., 2020)
66 climate conditions.

67 The aerosol module in the RegCM4 (Solomon et al., 2006; Zakey et al., 2006) considers
68 various aerosol life cycle processes, such as emission (source), advection, horizontal and
69 vertical diffusion, transport, conversion of hydrophobic to hygroscopic species and wet and dry
70 deposition (sink) (see Methods for more details). Previous studies (Das et al., 2016; Nair et al.,
71 2012) have pointed out that the RegCM4 underestimates the anthropogenic aerosol loading
72 over the Indian subcontinent, and therefore, the net aerosol impact over the region is dominated
73 by natural aerosols (Das et al., 2020). We recently implemented a dynamic ageing scheme in
74 the RegCM aerosol module (Ghosh et al., 2021), which converts carbonaceous aerosols from
75 hydrophobic to hygroscopic states based on the aerosol number concentration. Compared to
76 the constant conversion rate of 27.6 hours used in the default version of the model, the scheme
77 allowed a faster conversion in the polluted regions than in the clean areas of the South Asia
78 region. This, in turn, affected the aerosol forcing due to the changes in aerosol loadings induced
79 by the new hydrophobic-to-hygroscopic conversion scheme. It was also found that
80 implementing the dynamic ageing scheme alone is not sufficient to fully improve the model
81 performance and hypothesized that much of the model uncertainty was due to the emission
82 inventory.

83 In this work, we examined the changes in carbonaceous aerosol burden and their impact on
84 the radiation budget of the South Asia region due to the combined impact of the improved
85 dynamic ageing scheme and a regional emission inventory (Pandey and Venkataraman, 2014;
86 Sadavarte and Venkataraman, 2014) replacing the global emission inventory used in the default
87 model version (see Methods). We carried out four sets of simulations for the year 2010 - (1)
88 control simulation with the default (fixed) ageing scheme and global inventory (hereafter
89 Default_Sc), (2) simulation with the dynamic ageing scheme and global inventory
90 (Dyn_global), (3) simulation with the default ageing scheme and regional inventory
91 (Fix_Regio) and (4) simulation with the dynamic ageing scheme and regional emission
92 inventory (Dyn_Regio). The changes due to ageing alone (i.e., Default_Sc vs. Dyn_global)
93 have already been reported in Ghosh et al. (2021). Here we analyse and report the
94 improvements in model performance due to the combined impact of incorporating a better
95 emission inventory and a more realistic ageing scheme relative to the default model
96 configuration (i.e., Default_Sc vs. Dyn_Regio) and investigate these performance changes in
97 terms of the aerosol processes considered in the model. However, the changes due to emission
98 alone (i.e., Default_Sc vs. Fix_Regio) will be considered as an intermediate step towards
99 Dyn_Regio.

100 **2. Data and Methodology**

101 **2.1 Model configuration**

102 RegCM version 4 is a hydrostatic, compressible, primitive equation and sigma-p vertical
103 coordinate model with a dynamical core from the NCAR Mesoscale Model Version 5 (MM5)
104 (Grell et al., 1994). We have used the Community Climate Model Version 3 (CCM3) (Kiehl et
105 al., 1996) radiative transfer scheme with the modifications described in the literature (Giorgi
106 et al., 2012). The model is interactively coupled with both natural (dust and sea salt) (Zakey et
107 al., 2006, 2008) and anthropogenic aerosols (Solomon et al., 2006), along with a gas-phase
108 chemistry module (Shalaby et al., 2012), but for this study, we have only considered the
109 anthropogenic module (Solomon et al., 2006). The choice of parameterisation schemes for our
110 experiments has been provided in the following table:

Land surface processes	Biosphere-Atmosphere Transfer Scheme (BATS) (Dickinson et al., 1993)
Planetary boundary layer	University of Washington (UW) scheme (Grenier and Bretherton, 2001; Bretherton et al., 2004; O'Brien et al., 2012)
Cumulus convection scheme	Emanuel (Emanuel and Živković-Rothman, 1999) over land and Tiedtke (Tiedtke, 1993) over the ocean
Large-scale cloud and moisture process	SUBEX scheme (Pal et al., 2007, 2000)
Aerosol module	SUCA (Solomon et al., 2006)
Emission inventories	IIASA and IIT Bombay 2010

112
113 The anthropogenic aerosol module consists of sulphate, hydrophilic and hydrophobic BC,
114 and hydrophilic and hydrophobic OC, along with a sulphate scheme (Qian et al., 2001). The
115 mass concentrations of these species are tracked, assuming that they form an external mixture.
116 The emitted carbonaceous aerosols are considered to be 80 % hydrophobic and 20 %
117 hydrophilic for BC, while equal fractions of hydrophobic and hydrophilic OC are considered
118 in the simulations. The rate of change of mass mixing ratios of hydrophobic and hydrophilic
119 tracers, indicated by subscript 'hb' and 'hl,' is described by the chemical transport equation in
120 Solomon et al. (2006).

121 The atmospheric lifetime of aerosols is governed by dry and wet deposition. The dry
122 deposition velocity depends on the type of surface, while the dry deposition flux variation is

123 proportional to the tracer concentration in the lowest level of the model (around 30 m above
124 the surface). Wet deposition in the RegCM4 has been split into “in-cloud” and “below-cloud”
125 terms. The in-cloud removal process starts for large-scale clouds if the liquid water is higher
126 than the threshold level (0.01 g m^{-3}) in the model layers where the cloud fraction is more than
127 zero and is a function of the fractional removal rate of liquid water (fraction of precipitating
128 rain over liquid water content of the atmospheric layer, the in-cloud removal rate for cumulus
129 clouds is constant and fixed at 0.001 s^{-1}) and the aerosol solubility. This solubility is different
130 for different species, and thus hydrophilic and hydrophobic BC/OC have different in-cloud wet
131 deposition rates. The below-cloud washing out of the aerosols is controlled by their effective
132 diameters and densities. Collection efficiency for each aerosol species is computed from the
133 aerosol effective diameter and density, which is different for different species. The changes in
134 wet and dry deposition alter the ratio of hydrophobic to hydrophilic changes, which in turn
135 alters the atmospheric lifetime of aerosols. A detailed explanation regarding these changes due
136 to ageing alone can be referred to Ghosh et al. (2021). Seasonal variation in the lifetime of
137 particles, at the surface and upper atmosphere, due to ageing alone has been already explained
138 in Ghosh et al. (2021).

139 The model was simulated over the South-Asian CORDEX domain (Giorgi et al., 2009) [20°
140 S - 50° N and 10° - 130° E] for the year 2010 at $0.25^\circ \times 0.25^\circ$ resolution, while the results are
141 analysed over the Indian subcontinent [0° - 45° N and 60° - 105° E] with special focus on the IGP
142 [25° - 30° N and 73° - 89° E] and PI [8° - 20° N and 72° - 85° E]. The model consists of 18 vertical
143 levels with 50hPa as the model top pressure. There are three levels (1000, 925, 850 hPa) within
144 the boundary layer. ERA-Interim reanalysis dataset, at 1.5° resolution and 6-hourly temporal
145 resolution, has been used to generate the initial and lateral meteorological boundary conditions
146 for the study (Dee et al., 2011). The sea surface temperature was derived from the NOAA
147 Optimum Interpolated weekly $1^\circ \times 1^\circ$ gridded data and the chemical boundary conditions from
148 MOZART 6-hourly data. Four sets of simulations have been performed for the year 2010 - (1)
149 control simulation with the default (fixed) ageing scheme and global inventory (hereafter
150 Default_Sc), (2) simulation with the dynamic ageing scheme and global inventory
151 (Dyn_global), (3) simulation with the default ageing scheme and regional inventory
152 (Fix_Regio) and (4) simulation with the dynamic ageing scheme and regional emission
153 inventory (Dyn_Regio). In each of the experiments, the model was simulated from October 01,
154 2009, to December 31, 2010. The first three months were considered spin-up and thus were not
155 included in the analysis. The focus of this manuscript is the Indian landmass only. Changes in

156 aerosol properties over the oceans have not been discussed because the oceanic condition is
157 mostly clean with low tracer concentration compared to that over the landmass. In the
158 supplementary material Fig S1, there are hardly any emissions over the oceans. Additionally,
159 in (Ghosh et al., 2021), it is evident that the ageing time of the carbonaceous aerosols over the
160 oceans is larger than the default ageing timescale.

161

162 **2.2 Emission inventories**

163 In this study, we considered a global emission inventory
164 [https://www.iiasa.ac.at/web/home/research/researchPrograms/air/Global_emissions.html]
165 and a regional emission inventory (Pandey and Venkataraman, 2014; Sadavarte and
166 Venkataraman, 2014; Venkataraman, 2018). Figure S2 represents the seasonal variation of the
167 emissions estimated by the two inventories. The global emission inventory used in the
168 experiments ‘Default_Sc’ and ‘Dyn_global’ was developed by the IIASA emission inventory
169 at a resolution of $0.5^\circ \times 0.5^\circ$
170 [https://www.iiasa.ac.at/web/home/research/researchPrograms/air/Global_emissions.html].
171 The key emission sectors considered in this inventory are energy, industry, solvent use,
172 transport, domestic combustion, agriculture, open burning of agricultural waste, and waste
173 treatment. The emission estimates were available only at an annual scale with no seasonal
174 variation from 1990-2010.

175 The regional emission inventory used in experiments ‘Fix_regio’ and ‘Dyn_regio’ was
176 developed by IIT Bombay (Pandey and Venkataraman, 2014; Sadavarte and Venkataraman,
177 2014; Venkataraman et al., 2018) at a horizontal resolution of $0.25^\circ \times 0.25^\circ$ and the estimates
178 vary at a monthly scale. Thus, the regional emissions have a profound seasonal variability
179 (Figure S1). The key sectors included in the regional inventory are energy (coal + oil + gas),
180 heavy and light industry, brick production, residential cooking, solid biomass fuel, residential
181 cooking (LPG and kerosene), residential lighting (kerosene lamp), residential water heating,
182 residential space heating, informal industry, agricultural residue burning, on-road gasoline, on-
183 road diesel, railway, agricultural diesel pump, agricultural tractors. Among these sectors,
184 residential water heating, residential space heating, and agricultural residue burning sectors
185 have seasonality in emissions.

186

187 **2.3 In-situ BC data**

188 In-situ BC data for the year 2010 has been procured from 24 sites to evaluate the model
189 performance. These sites have been shown in the supplementary Fig S4. 21 of these sites are
190 part of the Indian Space Research Organization's Aerosol Radiative Forcing over India
191 Network, ARFINET (Babu et al., 2013; Gogoi et al., 2021). This network has been measuring
192 columnar AOD and BC for many years. In addition to the ARFINET, BC concentrations are
193 also measured independently at Kanpur (Tripathi et al., 2005) (entire 2010 except during the
194 monsoon season), Gadanki (Gadhavi et al., 2015; Jain et al., 2018), and Delhi (October-
195 December 2010) by individual institutions. In all the sites, BC was measured by an
196 Aethalometer. An aethalometer measures the amount of attenuation of the light beam passing
197 through the filter where particles get deposited. BC mass concentration is measured by the
198 change in optical attenuation given by the rate of BC deposition on the filter tape (Hansen et
199 al., 1984). Dataset from all the sites except Gadanki (monthly values) are available on a daily
200 scale and have been averaged to get the annual concentrations.

201

202 **2.4 MERRA-2 data**

203 Model simulated BC and OC columnar burdens have been evaluated against MERRA-2
204 reanalysis data. MERRA-2 is an updated reanalysis of atmospheric data produced by the NASA
205 Global Modeling and Assimilation Office (Buchard et al., 2017). MERRA-2 consists of
206 parameters that are not available in its predecessor, MERRA. It includes updates of the
207 Goddard Earth Observing System model and analysis scheme in order to give a more realistic
208 view of the ongoing climate analysis beyond MERRA's jargon. This dataset addressed the
209 limitations of MERRA. Various improvements in MERRA-2 include assimilation of aerosol
210 observations and improved representation of stratosphere, including ozone and cryosphere.
211 MERRA-2 data products are freely accessible through the NASA Goddard Earth Sciences Data
212 Information Services Center. We note that MERRA-2 data are also not observations and direct
213 validation of the MERRA-2 columnar BC and OC burden is not possible.

214

215 **2.5 MISR aerosol data**

216 MISR on-board Terra satellite crosses the equator around 10:30 hrs local time. It has a high
217 spatial resolution and a wide range of viewing angles. It views the Earth using four spectral
218 bands in each of the nine cameras and has a weekly global coverage between $\pm 82^\circ$. A detailed
219 description is provided in the literature (Diner et al., 1998). MISR-AOD has a correlation
220 coefficient of ~ 0.9 (for maritime sites) and ~ 0.7 (for dusty sites) w.r.t AERONET (Kahn et al.,

221 2005). In the absence of any direct measurement of anthropogenic AOD, we use MISR fine
222 AOD (AOD for particles smaller than 0.35 μm) (Dey and Di Girolamo, 2010).

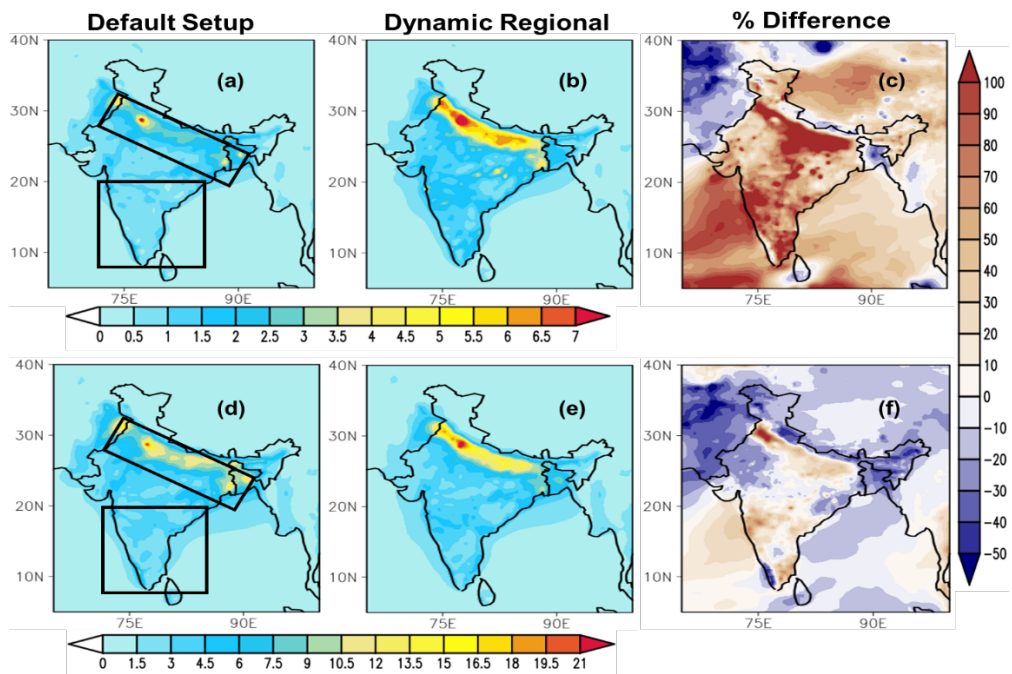
223

224 **3. Results**

225 In this section, we have discussed the three-dimensional annual distribution of
226 carbonaceous aerosols (sections 3.1 and 3.2) for the default (Default_Sc) and augmented
227 (Dyn_regio) model set-up. The seasonal distributions for all four experiments – Default_Sc,
228 Dyn_global, Fix_regio, and Dyn_Regio, have been reported in the supplementary information
229 (SI). In section 3.3, we have investigated the annual changes in aerosol optical properties due
230 to the default (Default_Sc) and augmented (Dyn_regio) model set-up. In this case, also, the
231 seasonal variability across the four experiments has been shown in the SI.

232 **3.1 Spatial distribution of carbonaceous aerosols**

233 Figure 1 shows the spatial distributions of the annual surface concentration for BC and OC
234 using the default and augmented model, along with their differences. Several key features are
235 notable. First, the OC concentration is almost three times higher than the BC concentration in
236 the augmented model, consistent with the literature (Priyadarshini et al., 2019). Secondly, the
237 concentrations are 2-3 times higher over the polluted Indo-Gangetic Plain (IGP) compared to
238 the rest of India in the augmented model. High aerosol loadings in the IGP are a result of the
239 combined effects of greater source strength, low topography surrounded by highlands to the
240 north and south, and unfavourable meteorology (Dey and Di Girolamo, 2010; Srivastava et al.,
241 2012). Thirdly, the BC and OC concentrations increase by >100 % and >60 %, respectively,
242 over the IGP and by smaller margins elsewhere in the augmented model relative to the default
243 configuration. The increase in the annual tracer concentrations can be further explained by the
244 seasonal distributions and the selected model configuration. To begin with, an increase in both
245 BC and OC concentrations during the winter (JF), pre-monsoon (MAM), and post-monsoon
246 (OND) seasons are clearly visible in [Fig S2](#) and [Fig S3](#) (see Supplementary Information SI).
247 During the monsoon, precipitation removes large amounts of aerosols; as a result, the increase
248 in BC concentration is almost negligible, and for OC, it is negative. The transition in
249 concentration from Dyn_global to Fix_regio is most prominent than that from Default_Sc to
250 Dyn_global or Fix_regio to Dyn_Regio. This indicates the impact of the switch from the global
251 to regional emission inventory ([Figure S1](#)) is greater than the impact of the implementation of
252 the dynamic ageing scheme (Figure S1) on the increases in BC and OC mass concentrations in
253 the augmented model.

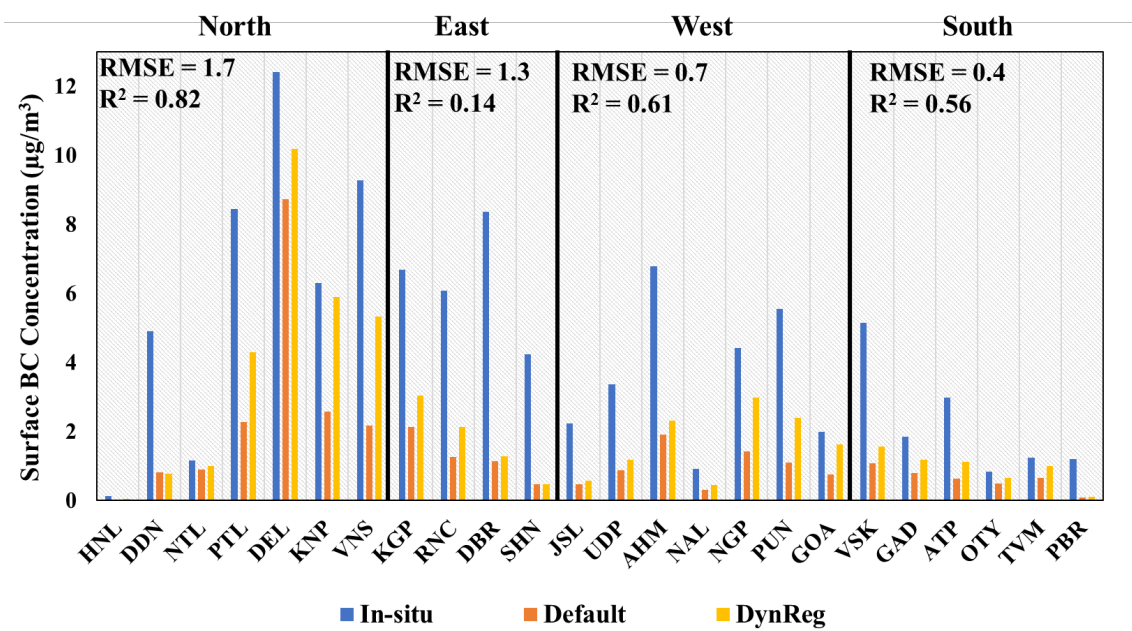


257 **Figure 1** Spatial distribution of surface mass concentration ($\mu\text{g m}^{-3}$) of BC (a, b) and OC (d, e)
 258 in 2010 over the Indian subcontinent using (left) the default and (middle) the augmented model
 259 configurations. Figures 1c and 1f represent the corresponding percentage differences due to the
 260 augmented model set-up (positive values imply an increase in mass concentration). The vertical
 261 distributions (shown in Figure 3) are analysed for the IGP and PI sub-regions marked by boxes
 262 in the panels of the left column.

264 We evaluate the performance of the customized model against BC surface concentrations
 265 measured at 24 sites across India (Figure 2). We note that the in-situ concentrations are point
 266 measurements, while the model grids containing these sites are representative of 25 km by 25
 267 km areas. The default model severely underestimates the surface BC compared to the in-situ
 268 observations (mean normalized bias, MNB = -69 %). Though the underestimation persists in
 269 the augmented model (by varying proportions across the sites), the simulated concentration
 270 magnitudes are closer to the observations (MNB = -51 %), particularly in the mega-cities of
 271 the polluted IGP (e.g., Delhi, Kanpur, Varanasi, Kharagpur). The improvement is small in some
 272 cities, particularly in the East India region (e.g., Dehradun, Dibrugarh, Ahmedabad), where the
 273 differences in global and regional emission inventories are also small. This suggests that the

274 problem could be related to the emission fluxes. In several cities, especially in the North and
 275 South Indian regions (e.g., Goa, Nainital, Ooty, Thiruvananthapuram), the simulated BC using
 276 the augmented model is a very close match with the observations. Overall, the augmented
 277 model ($R^2 = 0.66$) performs better than the default model ($R^2 = 0.6$) in simulating surface BC
 278 concentrations, and the errors shown in Figure 2 could also be amplified by the fact that the
 279 model data refers to a $25 \text{ km} \times 25 \text{ km}$ area as a single grid.

280



281

282

283 **Figure 2** Comparison of simulated BC surface concentration ($\mu\text{g m}^{-3}$) using the default and
 284 augmented model with in-situ measurements from 24 cities across India. Locations of the cities
 285 are shown in Figure S4. RMSE (in $\mu\text{g m}^{-3}$) and R^2 between the customized model simulations
 286 and surface measurements are also provided.

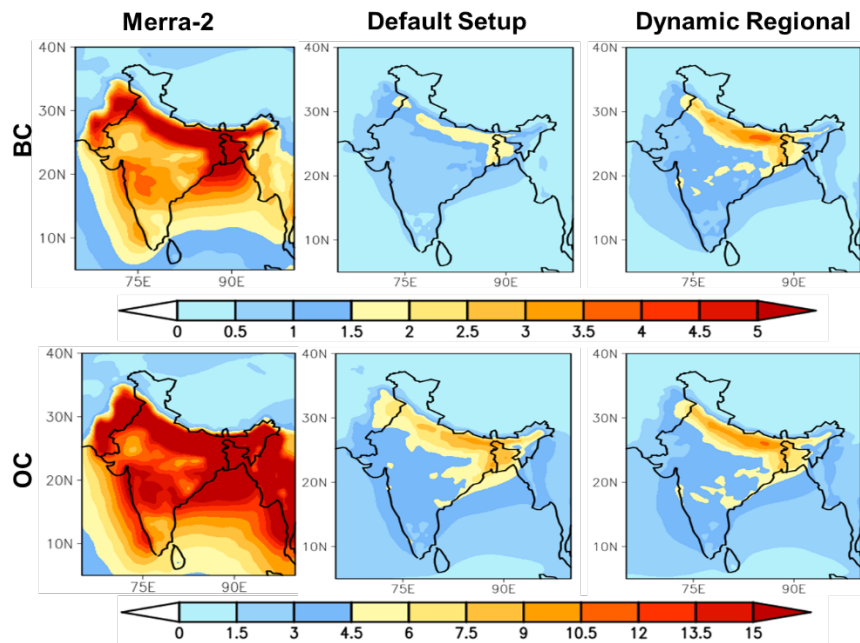
287

288 Since there are no in-situ measurements of columnar burden, we compare the simulated
 289 columnar burden (Figure 3) with data from Modern-Era Retrospective Analysis for Research
 290 and Applications, version 2 (MERRA-2) (Buchard et al., 2017). Similar to the surface mass
 291 concentration, the BC burden shows a more pronounced change than the OC burden due to the
 292 inclusion of the new model features. Here also, the introduction of the emissions alone played
 293 a more prominent role than the dynamic ageing alone (see Figure S5 and Figure S6 in SI), but
 294 the highest change can be observed in the presence of both. Though the simulated burden is

295 still underestimated relative to the MERRA-2 data, the values in the augmented model are
296 much closer to the reanalysis data, and the sequence of changes (in both BC and OC) follow
297 Dyn_Regio > Fix_Regio > Dyn_Global > Default_Sc. During the winter season (Jan-Feb), the
298 percentage difference of model-simulated column burden (w.r.t. MERRA-2) decreases from
299 >70 % to ~35 % for BC and from ~63 % to ~49 % for OC in the augmented model ([Figure S5](#)
300 and [S6](#)). A similar improvement is found in the pre-monsoon season (Mar-May). The higher
301 BC loading over the IGP results from higher magnitudes of regional emissions coupled with
302 faster ageing and slower removal rate. The percentage difference increases for OC burden over
303 northwest India decreases over the IGP and is negligible over the rest of the country. A probable
304 explanation for such OC distribution relies on the emission inventories used since the OC
305 emissions are slightly higher in the global inventory than those in the regional inventory over
306 northwest India and lower in the IGP. Emissions over the PI are roughly similar in the two
307 inventories ([Figure S1](#)). The role of emissions in both BC and OC simulated burden is further
308 supported by the observed transition changes from Dyn_Global to Fix_Regio. We also note that
309 anthropogenic aerosol emissions vary on an annual basis in MERRA-2 (Buchard et al., 2017);
310 hence, there could be larger uncertainties at a seasonal scale.

311 During the monsoon season (Jun-Sep), the BC loading increases, and OC loading decreases
312 in magnitude in the augmented model compared to the default set-up ([Figure S5](#)), mostly due
313 to the implementation of the regional inventory. The magnitude of the simulated BC column
314 burden is comparable between the Default_Sc and Dyn_sc experiments and that between the
315 Fix_Regio and Dyn_Regio ([Figure S5](#)), with an opposite pattern found for the OC column
316 burden ([Figure S6](#)). Two possible reasons can explain this result. First, the OC emissions in the
317 global inventory are higher than in the regional ones ([Figure S1](#)). Second, the model assumes
318 that OC is 50 % hydrophobic and 50 % hydrophilic at the time of emission (for BC, it is 80 %
319 hydrophobic and 20 % hydrophilic), and therefore the faster conversion to hydrophilic OC due
320 to the dynamic ageing can enhance the hydrophilic OC removal by rain. On analysing the wet
321 removal (refer to [Figure S7](#) and [Figure S8](#) in SI), BC_HL showed the expected highest removal
322 during JJAS, but OC_HL showed a lower magnitude of wet removal. Therefore, lower OC
323 emissions in the regional inventory play a major role, during JJAS, in simulating OC burden in
324 the augmented model. In the post-monsoon season (Oct-Dec), an overall increase in column
325 burden in the augmented model is observed throughout India. Higher emissions (in the case of
326 the regional inventory) result in higher concentrations of available condensing and coagulating
327 particles, which in turn allows faster ageing of hydrophobic to hydrophilic BC leading to

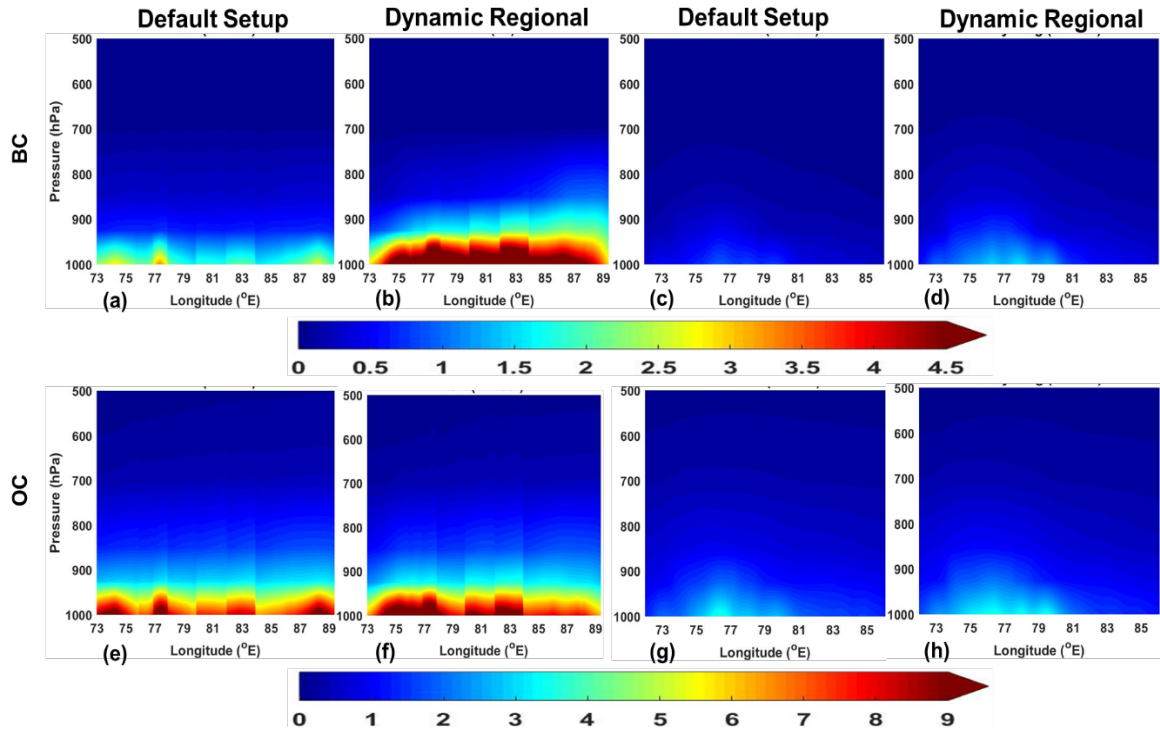
328 accumulation of BC particles in the atmosphere before their removal by dry deposition. The
329 changes in the OC loading are negligible in this season (refer to Figure S6 in SI).



330
331 **Figure 3** Comparison of spatial patterns of annual (top panel) BC and (bottom panel) OC
332 column burden (mg m^{-2}).
333

334 **3.2 Vertical distribution of carbonaceous aerosols**

335 In this section, we analyse the effects of the model improvements on the vertical
336 distribution of aerosols over the IGP and compare the results with the contrasting PI region,
337 where the emissions are much lower. The two regions are indicated by the boxes in Figure 1.
338 Figure 4 represents longitude-altitude cross-sections of annual BC and OC mass concentration
339 ($\mu\text{g m}^{-3}$) over the regions. The vertically distributed mass concentrations ($\mu\text{g m}^{-3}$) of both BC
340 and OC increase due to the model improvements up to 500 hPa. Similar to spatial distribution,
341 here also seasonal variability will help to explain the annual vertical concentrations.
342 Furthermore, the changes are more dramatic and prominent over IGP than that over PI.
343



344

345

346 **Figure 4** Longitude (in $^{\circ}$ E)-altitude (in hPa) cross-sections of (top panel) BC and (bottom panel) OC mass concentration ($\mu\text{g m}^{-3}$) over the IGP (a, b, e, f) and PI (c, d, g, h) for the default and customized model.

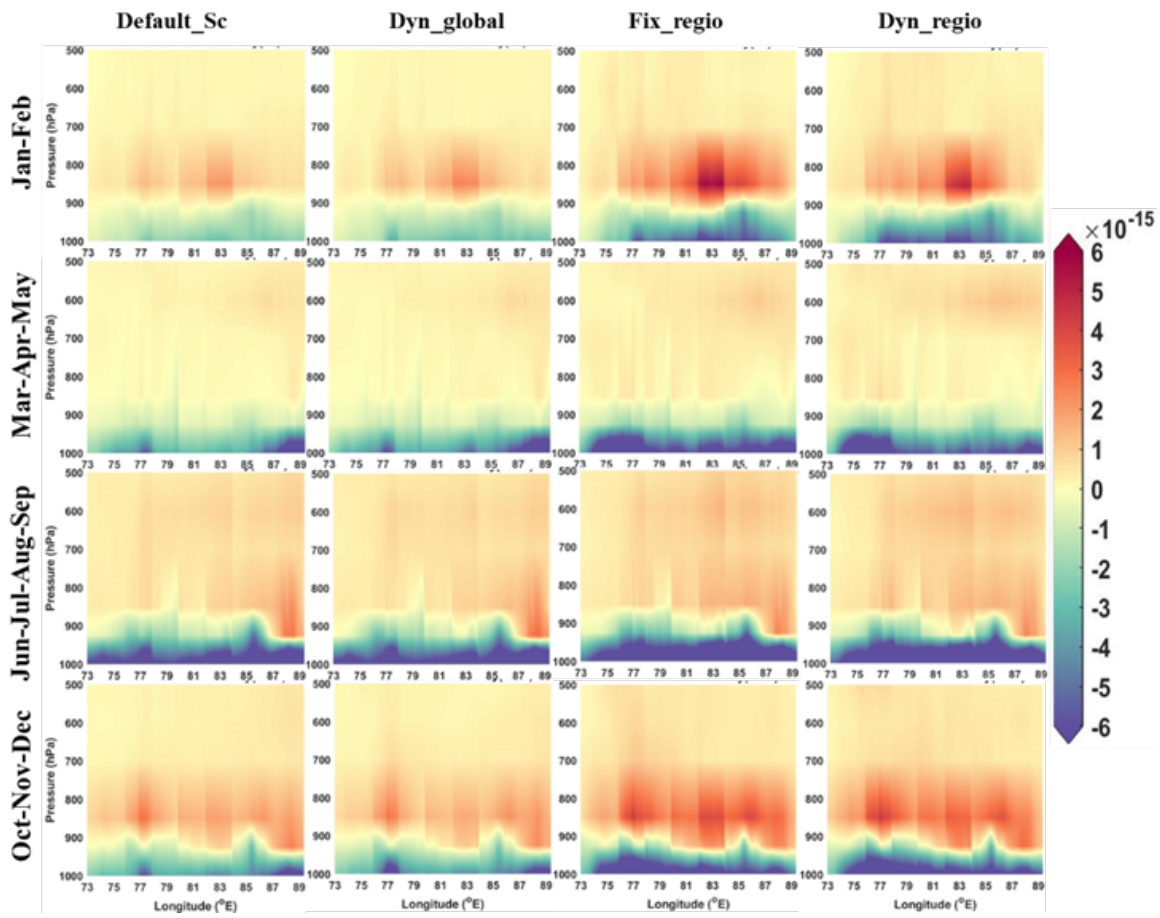
349

350 Over IGP, a larger increase is observed during the winter and post-monsoon seasons
 351 (Figures S9 and S10). Both the BC and OC concentrations ($\mu\text{g m}^{-3}$) are comparable in the
 352 default and Dyn_global configurations, but they increase in the Fix_regio and Dyn_regio set-
 353 ups (Figures S9 and S10). In these two seasons, both BC and the OC are distributed up to the
 354 mid-tropospheric levels but with differing magnitudes. This is indicative of higher
 355 concentrations of OC vertical transport than that of BC. During the pre-monsoon season, the
 356 vertical distributions of both BC and OC show responses similar to that of their spatial
 357 distributions. In the monsoon season, the tracer concentration is mainly confined to the surface
 358 levels, indicating a lower wet removal and slower ageing above 1000 hPa (Ghosh et al., 2021).

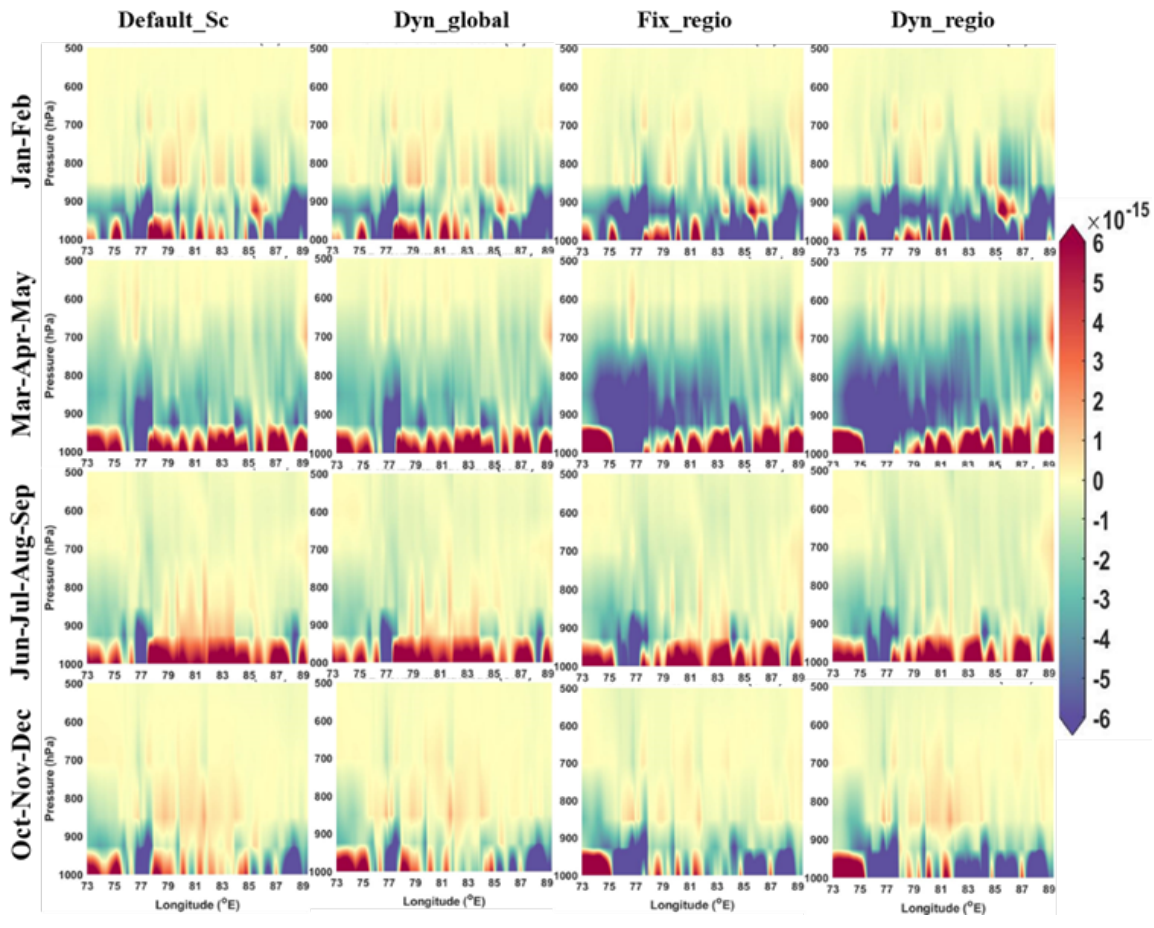
359 For further clarification of the seasonality of the vertical pumping effect, the convective
 360 tendency (represents vertical transport) and lateral advection (represents horizontal transport)
 361 have been investigated. The model simulated convective tendency and lateral advection
 362 (responsible for long-range transport) are given below. More positive values indicate a strong
 363 updraft above the surface due to convection. Convection tendency gradually increases from
 364 left to right (Figure 5 for BC and Figure S11 in SI for OC). Particularly in the drier seasons

365 since more particles are available in the absence of washout. During winter, the augmented
366 model (Dyn_Regio) shows a lesser pumping effect over IGP than that when only emissions
367 have been changed (Fix_Regio). This can be due to the fact that in the presence of dynamic
368 ageing a greater number of hydrophilic tracers are available for removal (evident from the
369 removal plot of BC_HL) even for a small amount of precipitation from western disturbances.
370 However, during post-monsoon (OND), due to negligible precipitation over IGP, removal rates
371 of hydrophilic tracers are comparable, and hence the pumping effect also follows the same
372 trend. A similar trend in convective tendency is also shown by OC particles (Figure S11 in SI).
373 The magnitude of OC convection tendency is stronger than that of BC particles, probably due
374 to a higher concentration (Priyadarshini et al., 2019; Ram et al., 2010) of available particles.
375 Besides, lateral advection is an indicator of horizontal long-range aerosol transport. More
376 positive values indicate strong flow along the surface due to advection. Advection shows strong
377 seasonality (from top to bottom – Figure 6 for BC and Figure S12 in SI for OC). In drier months
378 (JF and OND), horizontal transport is comparatively less than in pre-monsoon (MAM) and
379 monsoon (JJAS). Therefore, vertical convection is more prominent in dry seasons while
380 horizontal advection is dominant for MAM and JJAS, irrespective of the choice of schemes.
381 Consequently, the observed BC concentration is due to convection in JF and OND and due to
382 advection in MAM and JJAS. Similar logic can be applied for OC concentration distribution
383 due to lateral advection (Figure S12 in SI). However, the positive advection signal is stronger
384 than that of BC particles. This can be again due to the higher concentration of available particles
385 for transport to other regions.

386 In addition, the atmospheric profiles over the region have also been used to explain the tracer
387 distribution. In terms of changes in temperature profile, higher temperatures over IGP during
388 MAM and JJAS facilitated the strong vertical wind movement (negative values in Figure S13).
389 But negative convective tendency (Figure 5 for BC and Figure S24 in SI for OC) and positive
390 lateral advection of (Figure 6 for BC and Figure S23 in SI for OC) carbonaceous aerosols
391 during these months lowered their concentrations. This is further supported by the high RH
392 values particularly in JJAS (Figure S14) which resulted in higher removal. Exactly opposite is
393 happening during the drier months (JF and OND). Comparatively low temperatures (Figure
394 S15), facilitated more stable wind movement (positive values in Figure S13). However, in
395 presence of high emissions, the aerosol pumping effect resulted in strong convective tendency
396 (Figure 5) which further facilitated the higher concentrations during these months. The low RH
397 values (Figure SX2) during these months are also conducive of higher aerosol atmospheric
398 lifetime.



402 **Figure 5** Seasonal distribution of convective tendency ($\text{kg kg}^{-1} \text{ s}^{-1}$) of BC over IGP for four
403 distinct experiments.



405
406
407 **Figure 6** Seasonal distribution of lateral advection ($\text{kg kg}^{-1} \text{ s}^{-1}$) of BC over IGP for four distinct
408 experiments.
409

410 Over the PI, the annual concentrations of carbonaceous aerosols (Figure 4) are very low
411 than over the IGP, which limits the impact of dynamic ageing because of the lower availability
412 of condensing and coagulating particles (relative to the IGP). This results in a slower ageing
413 and lower accumulation of hydrophilic tracers in the troposphere. However, the vertical
414 pumping effect is quite prominent during the winter season in the augmented configuration
415 (Figures S16 and S17). During the pre-monsoon season, only the BC concentration shows an
416 increment in the lower troposphere, while the OC concentration remains more or less
417 unchanged. The PI receives rainfall during the southwest and northeast monsoon; hence the
418 tracer concentration is further lowered during the monsoon and post-monsoon seasons. This is
419 further supported by the high relative humidity values over PI during monsoon and post-
420 monsoon (Figure S18). The high humidity during JJAS can also influence a comparatively
421 high, near surface air temperature (Figure S19) by trapping the radiation. This in turn resulted

422 in a high vertical wind shear (Figure S20) over PI during this season. But the convective
423 tendency is low for both BC and OC (Figure S21 and S24 respectively).

424 The lower concentration can be, therefore, primarily because of the lower emissions for both
425 BC and OC (refer to Figure S1). This argument is further supported by lower washout than IGP
426 (Figure S7 and S8) in spite of high RH values (Figure S24). Since, the convective tendency, as
427 well as lateral advection for BC, is not playing any major role (as can be seen in Figure S21
428 and Figure S22 in SI), therefore again concluding the role of lower emissions. In the case of
429 OC, lateral advection (Figure S23 in SI) and comparatively lower emissions (Figure S1 in SI)
430 than IGP can be the predominant factors for lower concentration over PI in the presence of
431 negative convective tendency (Figure S24 in SI).

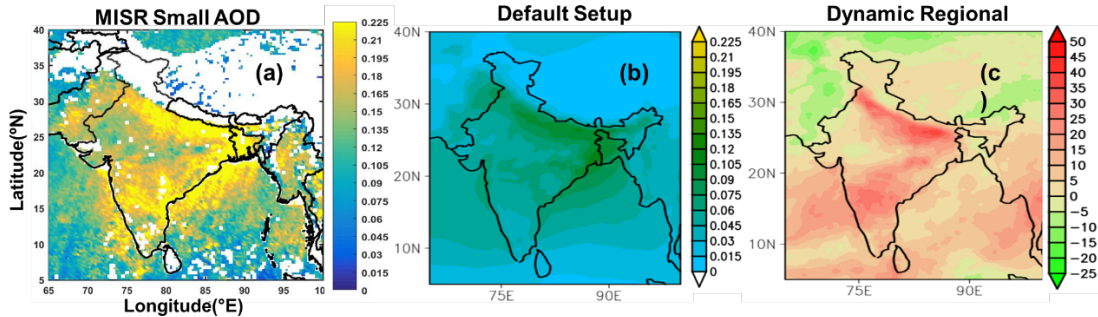
432

433 **3.3 Optical and radiative properties of anthropogenic aerosols**

434 We now examine the effects of the model improvements on the optical properties of
435 anthropogenic aerosols. In this regard, we note that the changes due to the implementation of
436 the dynamic ageing scheme can alter only BC and OC concentrations, while the changes related
437 to the emission inventory impact the sulphate concentration as well. We consider the AOD due
438 to small particles (radius $<0.35\text{ }\mu\text{m}$) from the Multiangle Imaging Spectroradiometer, MISR
439 (Kahn and Gaitley, 2015), as a proxy for anthropogenic AOD (hereafter AAOD) since direct
440 measurement of AAOD are not available to evaluate our model performance (Figure 7).

441 The simulated annual AAOD is $>50\text{ }\%$ lower than the MISR small-AOD over the polluted
442 IGP and 30-50 % lower over the PI in the default model. This is consistent with the previous
443 studies (Nair et al., 2012). These model underestimations improve by 25-35 % over the IGP
444 and parts of PI in the augmented model. The seasonal plots (Figure S8) clearly show an increase
445 in AAOD in all seasons except during the monsoon. This increase in AAOD is due to both the
446 implementation of region-specific emission fluxes (Nair et al., 2012) and the dynamic ageing
447 scheme (Ghosh et al., 2021). The AAOD still remains underestimated in some regions, which
448 can possibly be addressed by further improvements of the emission estimates, for example, the
449 addition of missing sectors (e.g., crematorium, municipal solid waste burning, etc.), improving
450 sectoral methodologies for informal activities and incorporation of regionally measured
451 emission factors.

452



453

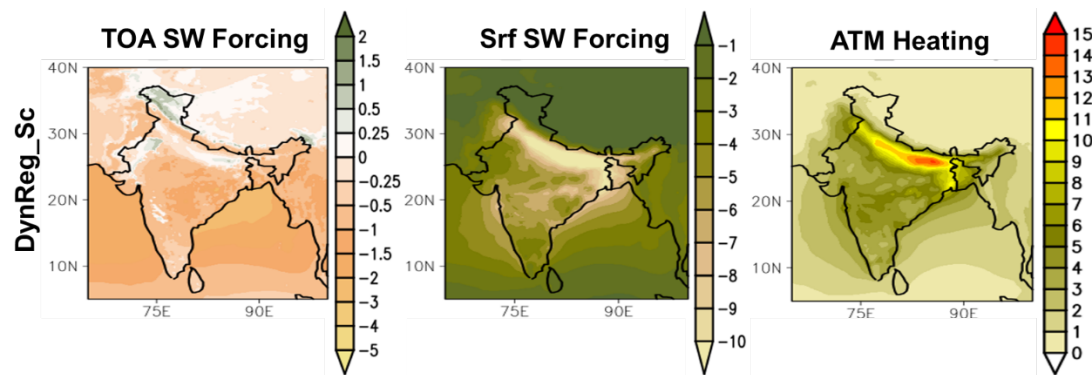
454 **Figure 7** Spatial distribution of (a) MISR small mode AOD ('white' color implies 'no data'),
 455 (b) AAOD simulated by default_sc, and (c) percentage increase in AAOD simulated by the
 456 augmented model w.r.t default_sc for 2010.

457

458 Spatial patterns of the annual top-of-the-atmosphere (TOA), surface, and atmospheric
 459 radiative forcing associated with the anthropogenic aerosols for the augmented model are
 460 shown in Figure 8. Currently, the model does not assume aerosol interaction with clouds;
 461 therefore, the radiative feedback is mainly governed by direct radiative forcing. Hence,
 462 secondary effects due to aerosols cannot be considered for the observed values in Fig 8. The
 463 TOA aerosol radiative forcing lies in the range of -0.5 to -1.5 W m^{-2} over most of the Indian
 464 landmass, except the IGP, where it is positive (0.25 to 1 W m^{-2}) due to the higher concentration
 465 of carbonaceous aerosols (Figure 1 and Figure 3), particularly BC. The TOA forcing is also
 466 positive over the Indian desert and snow-covered regions even when the carbonaceous aerosol
 467 concentrations are lower or comparable to the rest of India. The high surface albedo in these
 468 regions allows for an enhanced interaction of the carbonaceous aerosols with solar radiation,
 469 resulting in a warming effect (Satheesh, 2002). The surface radiative forcing is found to be
 470 larger than -10 W m^{-2} over the polluted IGP, which is consistent with published results
 471 (Ramanathan and Carmichael, 2008). Over the rest of India, the surface forcing values lie
 472 between -3 to -8 W m^{-2} . Due to the model improvements (forcing estimates with the default
 473 model are shown in Figure 8), the TOA forcing changes by -72.75 %, and the surface dimming
 474 increases by 39.73 % over the IGP and by -23.94 % and 34.35 %, respectively, over PI. As a
 475 result, the atmospheric heating increases by $\sim 9 \text{ W m}^{-2}$ over the IGP. The simulated surface
 476 shortwave radiation shows a statistically significant ($p < 0.05$) correlation with the observations
 477 from CERES (Su et al., 2005) all-sky and clear-sky radiation throughout the year except in
 478 MAM and JJAS clear-sky conditions (Figure S26 and S27). Here we didn't separate clear and
 479 cloudy days because the aerosol-cloud interactions are absent in the model. Therefore, the

480 reflection from clouds will also be lower. As a result, contribution to the observed AAOD (in
481 supplementary figure S25) due to cloud reflections will also be lower. Therefore, AAOD
482 distribution over IGB is primarily responsible for the surface dimming effect and the resulting
483 atmospheric heating.

484



485

486 **Figure 8** Annual variation of SW radiative forcing (W m^{-2}) at TOA (left column), at the surface
487 (middle column), and the resultant atmospheric heating (W/m^2) (right column) for the
488 customized set-up.

489

490 **4 Discussion and conclusions**

491 Accurate estimates of emission fluxes and a better representation of aerosol processes are
492 required to improve the representation of aerosol life-cycle and radiative effects in climate
493 models. Here we modified the regional climate model RegCM4 by implementing a dynamic
494 ageing scheme and a regional emission inventory and examined the combined impact of these
495 factors on the model performance over the Indian monsoon region. We note that though the
496 aerosol simulations improve due to these model enhancements, some systematic biases persist
497 (underestimation of carbonaceous aerosol concentrations) and need to be further addressed.
498 For example, RegCM has a bulk scheme for anthropogenic aerosols, and thus the number
499 concentration is calculated from the bulk mass concentration (Ghosh et al., 2021). The
500 anthropogenic aerosol module can thus be improved by including a particle size-dependent
501 representation. In addition, the present dynamic ageing timescale depends only on the
502 anthropogenic aerosol number concentration, while it should, in fact, depend on the total
503 (anthropogenic + natural) number concentrations. The simulations presented in this work did
504 not include natural aerosols, which could have impacted the meteorology through dynamic
505 feedback, possibly affecting the carbonaceous aerosol burden. This aspect will be examined in

506 future work. Thirdly, though the emission fluxes of BC, OC, and SO₂ are higher in the region
507 than the global inventory, there may still be uncertainty related to missing sectoral sources.

508

509 Our work demonstrates that even the improvement of some aspects of the aerosol
510 representation can lead to substantial enhancements in the model performance. We also find
511 that over the South Asian monsoon region, particularly over highly polluted regions such as
512 the IGP, the default model significantly underestimates the surface dimming and atmospheric
513 heating, which can have implications for climate studies (Das et al., 2016, 2020) and this
514 problem is substantially ameliorated with our model augmentations.

515 The key conclusions of our work can be summarized as follows.

- 516 1. The conclusion in the model RegCM4 of a dynamic ageing scheme and a regional
517 emission inventory substantially improves the model performance over the Indian sub-
518 continent.
- 519 2. The BC and OC surface concentration and column burden increase due to the model
520 improvements, more so as a combined effect of the two factors than because of the
521 individual ones.
- 522 3. The TOA, surface, and atmospheric radiative forcing are estimated to be -0.3, -5.3, and
523 5.0 W m⁻², respectively, over the polluted IGP using the augmented model, but they
524 could still be underestimated.

525

526 *Data availability.* The model RegCM4 code is freely available online from
527 (<https://gforge.ictp.it/gf/project/regcm/>). The anthropogenic aerosol emissions considered for
528 the simulations are taken from the IIASA inventory. The data used can be easily accessed
529 online at http://clima-dods.ictp.it/Data/RegCM_Data/RCP_EMGLOB_PROCESSED/iasa/
530 website. Input files for the RegCM4 model are archived on <http://clima->
531 clima-dods.ictp.it/Data/RegCM_Data/ website. MISR data is available freely from [https://www-](https://www-misr.jpl.nasa.gov/)
532 [misr.jpl.nasa.gov/](https://www-misr.jpl.nasa.gov/) while MERRA-2 data is freely available from the NASA Giovanni site
533 <https://giovanni.gsfc.nasa.gov/giovanni/>.

534

535 *Competing Interests.* All the authors declare that they have no conflict of interest.

536 *Acknowledgements.* We thank the Aerosol Radiative Forcing over India (ARFINET) project of
537 ISRO GBP for sharing the BC data. The authors thank the internal review committee of the
538 NCAP-COALESCE project for their comments and suggestions. The views expressed in this

539 document are solely those of the authors and do not necessarily reflect those of the Ministry.
540 The Ministry does not endorse any products or commercial services mentioned in this
541 publication. SG acknowledges the supercomputing facility Keeling of the University of Illinois
542 Urbana-Champaign. SD acknowledges IIT Delhi for the support for the Institute Chair
543 fellowship.

544

545 *Financial Support.* This work is supported by the MoEFCC under the NCAP-COALESCE
546 project [Grant 14/10/2014-CC]. SG acknowledges the support for the DST-INSPIRE
547 fellowship (IF150055) and Fulbright-Kalam Climate Doctoral Fellowship. NR acknowledges
548 funding from NSF AGS-1254428 and DOE grant DE-SC0019192. Funding from the
549 Department of Science and Technology – Funds for Improvement of Science and Technology
550 infrastructure in universities and higher educational institutions (DST-FIST) grant
551 (SR/FST/ESII-016/2014) is acknowledged for the computing support.

552

553 **References**

554

555 Ajay, P., Pathak, B., Solmon, F., Bhuyan, P. K., and Giorgi, F.: Obtaining best parameterization scheme
556 of RegCM 4.4 for aerosols and chemistry simulations over the CORDEX South Asia, 53, 329–352,
557 <https://doi.org/10.1007/s00382-018-4587-3>, 2019.

558 Babu, S. S., Manoj, M. R., Moorthy, K. K., Gogoi, M. M., Nair, V. S., Kompalli, S. K., Satheesh, S. K.,
559 Niranjan, K., Ramagopal, K., Bhuyan, P. K., and Singh, D.: Trends in aerosol optical depth over Indian
560 region: Potential causes and impact indicators, 118, 11,794-11,806,
561 <https://doi.org/10.1002/2013JD020507>, 2013.

562 Bond, T. C., Doherty, S. J., Fahey, D. W., Forster, P. M., Berntsen, T., Deangelo, B. J., Flanner, M. G.,
563 Ghan, S., Kärcher, B., Koch, D., Kinne, S., Kondo, Y., Quinn, P. K., Sarofim, M. C., Schultz, M. G.,
564 Schulz, M., Venkataraman, C., Zhang, H., Zhang, S., Bellouin, N., Guttikunda, S. K., Hopke, P. K.,
565 Jacobson, M. Z., Kaiser, J. W., Klimont, Z., Lohmann, U., Schwarz, J. P., Shindell, D., Storelvmo, T.,
566 Warren, S. G., and Zender, C. S.: Bounding the role of black carbon in the climate system: A scientific
567 assessment, 118, 5380–5552, <https://doi.org/10.1002/jgrd.50171>, 2013.

568 Bretherton, C. S., McCaa, J. R., and Grenier, H.: A New Parameterization for Shallow Cumulus
569 Convection and Its Application to Marine Subtropical Cloud-Topped Boundary Layers. Part I:
570 Description and 1D Results, 132, 864–882, [https://doi.org/10.1175/1520-0493\(2004\)132<0864:ANPFSC>2.0.CO;2](https://doi.org/10.1175/1520-0493(2004)132<0864:ANPFSC>2.0.CO;2), 2004.

572 Buchard, V., Randles, C. A., Silva, A. M. da, Darmenov, A., Colarco, P. R., Govindaraju, R., Ferrare, R.,
573 Hair, J., Beyersdorf, A. J., Ziemb, L. D., and Yu, H.: The MERRA-2 Aerosol Reanalysis, 1980 Onward.
574 Part II: Evaluation and Case Studies, 30, 6851–6872, <https://doi.org/10.1175/JCLI-D-16-0613.1>, 2017.

575 Das, S., Dey, S., Dash, S. K., Giuliani, G., and Solmon, F.: Dust aerosol feedback on the Indian summer
576 monsoon: Sensitivity to absorption property, 120, 9642–9652,
577 <https://doi.org/10.1002/2015JD023589>, 2015.

578 Das, S., Dey, S., and Dash, S. K.: Direct radiative effects of anthropogenic aerosols on Indian summer
579 monsoon circulation, 124, 629–639, <https://doi.org/10.1007/s00704-015-1444-8>, 2016.

580 Das, S., Giorgi, F., Giuliani, G., Dey, S., and Coppola, E.: Near-Future Anthropogenic Aerosol Emission
581 Scenarios and Their Direct Radiative Effects on the Present-Day Characteristics of the Indian Summer
582 Monsoon, 125, <https://doi.org/10.1029/2019JD031414>, 2020.

583 Dash, S. K., Mishra, S. K., Pattnayak, K. C., Mamgain, A., Mariotti, L., Coppola, E., Giorgi, F., and
584 Giuliani, G.: Projected seasonal mean summer monsoon over India and adjoining regions for the
585 twenty-first century, *Theor Appl Climatol*, 122, 581–593, <https://doi.org/10.1007/s00704-014-1310-0>, 2015.

587 Dee, D. P., Uppala, S. M., Simmons, A. J., Berrisford, P., Poli, P., Kobayashi, S., Andrae, U., Balmaseda,
588 M. A., Balsamo, G., Bauer, P., Bechtold, P., Beljaars, A. C. M., van de Berg, L., Bidlot, J., Bormann, N.,
589 Delsol, C., Dragani, R., Fuentes, M., Geer, A. J., Haimberger, L., Healy, S. B., Hersbach, H., Hólm, E. V.,
590 Isaksen, L., Kållberg, P., Köhler, M., Matricardi, M., McNally, A. P., Monge-Sanz, B. M., Morcrette, J. J.,
591 Park, B. K., Peubey, C., de Rosnay, P., Tavolato, C., Thépaut, J. N., and Vitart, F.: The ERA-Interim
592 reanalysis: Configuration and performance of the data assimilation system, 137, 553–597,
593 <https://doi.org/10.1002/qj.828>, 2011.

594 Dey, S. and Di Girolamo, L.: A climatology of aerosol optical and microphysical properties over the
595 Indian subcontinent from 9 years (2000–2008) of Multiangle Imaging Spectroradiometer (MISR)
596 data, 115, <https://doi.org/10.1029/2009JD013395>, 2010.

597 Dickinson, R., Henderson-Sellers, A., and Kennedy, P.: Biosphere-atmosphere Transfer Scheme
598 (BATS) Version 1e as Coupled to the NCAR Community Climate Model, UCAR/NCAR,
599 <https://doi.org/10.5065/D67W6959>, 1993.

600 Diner, D. J., Beckert, J. C., Reilly, T. H., Bruegge, C. J., Conel, J. E., Kahn, R. A., Martonchik, J. V.,
601 Ackerman, T. P., Davies, R., Gerstl, S. A. W., Gordon, H. R., Muller, J.-P., Myneni, R. B., Sellers, P. J.,
602 Pinty, B., and Verstraete, M. M.: Multi-angle Imaging SpectroRadiometer (MISR) instrument
603 description and experiment overview, 36, 1072–1087, <https://doi.org/10.1109/36.700992>, 1998.

604 Emanuel, K. A. and Živković-Rothman, M.: Development and Evaluation of a Convection Scheme for
605 Use in Climate Models, 56, 1766–1782, [https://doi.org/10.1175/1520-0469\(1999\)056<1766:DAEOAC>2.0.CO;2](https://doi.org/10.1175/1520-0469(1999)056<1766:DAEOAC>2.0.CO;2), 1999.

607 Gadhavi, H. S., Renuka, K., Ravi Kiran, V., Jayaraman, A., Stohl, A., Klimont, Z., and Beig, G.:
608 Evaluation of black carbon emission inventories using a Lagrangian dispersion model – a case study
609 over southern India, 15, 1447–1461, <https://doi.org/10.5194/acp-15-1447-2015>, 2015.

610 Ghosh, S., Riemer, N., Giuliani, G., Giorgi, F., Ganguly, D., and Dey, S.: Sensitivity of Carbonaceous
611 Aerosol Properties to the Implementation of a Dynamic Aging Parameterization in the Regional
612 Climate Model RegCM, 126, e2020JD033613, <https://doi.org/10.1029/2020JD033613>, 2021.

613 Giorgi, F., Jones, C., and Asrar, G. R.: Addressing climate information needs at the regional level: the
614 CORDEX framework, *WMO Bulletin*, 2009.

615 Giorgi, F., Coppola, E., Solmon, F., Mariotti, L., Sylla, M. B., Bi, X., Elguindi, N., Diro, G. T., Nair, V.,
616 Giuliani, G., Turuncoglu, U. U., Cozzini, S., Gütler, I., O'Brien, T. A., Tawfik, A. B., Shalaby, A., Zakey,
617 A. S., Steiner, A. L., Stordal, F., Sloan, L. C., and Brankovic, C.: RegCM4: Model description and
618 preliminary tests over multiple CORDEX domains, 52, 7–29, <https://doi.org/10.3354/cr01018>, 2012.

619 Gogoi, M. M., Babu, S. S., Arun, B. S., Moorthy, K. K., Ajay, A., Ajay, P., Suryavanshi, A., Borgohain, A.,
620 Guha, A., Shaikh, A., Pathak, B., Gharai, B., Ramasamy, B., Balakrishnaiah, G., Menon, H. B., Kuniyal,
621 J. C., Krishnan, J., Gopal, K. R., Maheswari, M., Naja, M., Kaur, P., Bhuyan, P. K., Gupta, P., Singh, P.,
622 Srivastava, P., Singh, R. S., Kumar, R., Rastogi, S., Kundu, S. S., Kompalli, S. K., Panda, S., Rao, T. C.,
623 Das, T., and Kant, Y.: Response of ambient BC concentration across the Indian region to the nation-
624 wide lockdown: results from the ARFINET measurements of, 120, 11, 2021.

625 Grell, G., Dudhia, J., and Stauffer, D.: A description of the fifth-generation Penn State/NCAR
626 Mesoscale Model (MM5), UCAR/NCAR, <https://doi.org/10.5065/D60Z716B>, 1994.

627 Grenier, H. and Bretherton, C. S.: A Moist PBL Parameterization for Large-Scale Models and Its
628 Application to Subtropical Cloud-Topped Marine Boundary Layers, 129, 357–377,
629 [https://doi.org/10.1175/1520-0493\(2001\)129<0357:AMPPFL>2.0.CO;2](https://doi.org/10.1175/1520-0493(2001)129<0357:AMPPFL>2.0.CO;2), 2001.

630 Hansen, A. D. A., Rosen, H., and Novakov, T.: The aethalometer — An instrument for the real-time
631 measurement of optical absorption by aerosol particles, *Science of The Total Environment*, 36, 191–
632 196, [https://doi.org/10.1016/0048-9697\(84\)90265-1](https://doi.org/10.1016/0048-9697(84)90265-1), 1984.

633 Jain, C. D., Gadhavi, H. S., Wankhede, T., Kallelapu, K., Sudhesh, S., Das, L. N., Pai, R. U., and
634 Jayaraman, A.: Spectral Properties of Black Carbon Produced during Biomass Burning, *Aerosol Air*
635 *Qual. Res.*, 18, 671–679, <https://doi.org/10.4209/aaqr.2017.03.0102>, 2018.

636 Kahn, R., Li, W.-H., Martonchik, J. V., Bruegge, C. J., Diner, D. J., Gaitley, B. J., Abdou, W., Dubovik, O.,
637 Holben, B., Smirnov, A., Jin, Z., and Clark, D.: MISR Calibration and Implications for Low-Light-Level
638 Aerosol Retrieval over Dark Water, 62, 1032–1052, <https://doi.org/10.1175/JAS3390.1>, 2005.

639 Kahn, R. A. and Gaitley, B. J.: An analysis of global aerosol type as retrieved by MISR, 120, 4248–
640 4281, <https://doi.org/10.1002/2015JD023322>, 2015.

641 Kanakidou, M., Seinfeld, J. H., Pandis, S. N., Barnes, I., Dentener, F. J., Facchini, M. C., Van Dingenen,
642 R., Ervens, B., Nenes, A., Nielsen, C. J., Swietlicki, E., Putaud, J. P., Balkanski, Y., Fuzzi, S., Horth, J.,
643 Moortgat, G. K., Winterhalter, R., Myhre, C. E. L., Tsigaridis, K., Vignati, E., Stephanou, E. G., and
644 Wilson, J.: Organic aerosol and global climate modelling: a review, 5, 1053–1123,
645 <https://doi.org/10.5194/acp-5-1053-2005>, 2005.

646 Kiehl, J., Hack, J., Bonan, G., Boville, B., Briegleb, B., Williamson, D., and Rasch, P.: Description of the
647 NCAR Community Climate Model (CCM3), UCAR/NCAR, <https://doi.org/10.5065/D6FF3Q99>, 1996.

648 Naik, V., Szopa, S., Adhikary, B., Artaxo Netto, P. E., Berntsen, T., Collins, W. D., Fuzzi, S., Gallardo, L.,
649 Kiendler-Scharr, A., Klimont, Z., Liao, H., Unger, N., and Zanis, P.: Short-lived climate forcers, in:
650 Climate Change 2021: The Physical Science Basis. Contribution of Working Group I to the Sixth
651 Assessment Report of the Intergovernmental Panel on Climate Change, edited by: Masson-Delmotte,
652 V., Zhai, P., Pirani, A., Connors, S. L., Péan, C., Berger, S., Caud, N., Chen, Y., Goldfarb, L., Gomis, M. I.,
653 Huang, M., Leitzell, K., Lonnoy, E., Matthews, J. B. R., Maycock, T. K., Waterfield, T., Yelekçi, Ö., Yu,
654 R., and Zhou, B., Cambridge University Press, 2021.

655 Nair, V. S., Solmon, F., Giorgi, F., Mariotti, L., Babu, S. S., and Moorthy, K. K.: Simulation of South
656 Asian aerosols for regional climate studies, 117, 4209, <https://doi.org/10.1029/2011JD016711>, 2012.

657 O'Brien, T. A., Chuang, P. Y., Sloan, L. C., Faloona, I. C., and Rossiter, D. L.: Coupling a new turbulence
658 parametrization to RegCM adds realistic stratocumulus clouds, 5, 989–1008,
659 <https://doi.org/10.5194/gmd-5-989-2012>, 2012.

660 Pal, J. S., Small, E. E., and Eltahir, E. A. B.: Simulation of regional-scale water and energy budgets:
661 Representation of subgrid cloud and precipitation processes within RegCM, 105, 29579–29594,
662 <https://doi.org/10.1029/2000JD900415>, 2000.

663 Pal, J. S., Giorgi, F., Bi, X., Elguindi, N., Solomon, F., Gao, X., Rauscher, S. A., Francisco, R., Zakey, A.,
664 Winter, J., Ashfaq, M., Syed, F. S., Bell, J. L., Differbaugh, N. S., Karmacharya, J., Konari, A., Martinez,
665 D., Da Rocha, R. P., Sloan, L. C., and Steiner, A. L.: Regional Climate Modeling for the Developing
666 World: The ICTP RegCM3 and RegCNET, 88, 1395–1410, <https://doi.org/10.1175/BAMS-88-9-1395>,
667 2007.

668 Pandey, A. and Venkataraman, C.: Estimating emissions from the Indian transport sector with on-
669 road fleet composition and traffic volume, *Atmospheric Environment*, 98, 123–133,
670 <https://doi.org/10.1016/j.atmosenv.2014.08.039>, 2014.

671 Pattnayak, K. C., Panda, S. K., Saraswat, V., and Dash, S. K.: Assessment of two versions of regional
672 climate model in simulating the Indian Summer Monsoon over South Asia CORDEX domain, 50,
673 3049–3061, <https://doi.org/10.1007/s00382-017-3792-9>, 2018.

674 Priyadarshini, B., Verma, S., Chatterjee, A., Sharma, S. K., and Mandal, T. K.: Chemical
675 characterization of fine atmospheric particles of water-soluble ions and carbonaceous species in a
676 tropical urban atmosphere over the eastern Indo-Gangetic plain, 19, 129–147,
677 <https://doi.org/10.4209/aaqr.2017.12.0606>, 2019.

678 Putaud, J.-P., Van Dingenen, R., Alastuey, A., Bauer, H., Birmili, W., Cyrys, J., Flentje, H., Fuzzi, S.,
679 Gehrig, R., Hansson, H. C., Harrison, R. M., Herrmann, H., Hitzenberger, R., Hüglin, C., Jones, A. M.,
680 Kasper-Giebl, A., Kiss, G., Kousa, A., Kuhlbusch, T. A. J., Löschau, G., Maenhaut, W., Molnar, A.,
681 Moreno, T., Pekkanen, J., Perrino, C., Pitz, M., Puxbaum, H., Querol, X., Rodriguez, S., Salma, I.,
682 Schwarz, J., Smolik, J., Schneider, J., Spindler, G., ten Brink, H., Tursic, J., Viana, M., Wiedensohler, A.,
683 and Raes, F.: A European aerosol phenomenology – 3: Physical and chemical characteristics of
684 particulate matter from 60 rural, urban, and kerbside sites across Europe, *Atmospheric Environment*,
685 44, 1308–1320, <https://doi.org/10.1016/j.atmosenv.2009.12.011>, 2010.

686 Qian1, Y., Giorgi1, F., Huang2, Y., Chameides2, W., and Luo2, C.: Regional simulation of
687 anthropogenic sulfur over East Asia and its sensitivity to model parameters, 53, 171–191, 2001.

688 Rai, P. K., Singh, G. P., and Dash, S. K.: Projected Change and Variability Assessment of Indian
689 Summer Monsoon Precipitation in South Asia CORDEX Domain Under High-Emission Pathway, 177,
690 3475–3499, <https://doi.org/10.1007/s00024-019-02373-3>, 2020.

691 Ram, K., Sarin, M. M., and Tripathi, S. N.: A 1 year record of carbonaceous aerosols from an urban
692 site in the Indo-Gangetic Plain: Characterization, sources, and temporal variability, 115,
693 <https://doi.org/10.1029/2010JD014188>, 2010.

694 Ramanathan, V. and Carmichael, G.: Global and regional climate changes due to black carbon, 1,
695 221–227, <https://doi.org/10.1038/ngeo156>, 2008.

696 Riemer, N., Ault, A. P., West, M., Craig, R. L., and Curtis, J. H.: Aerosol Mixing State: Measurements,
697 Modeling, and Impacts, 57, 187–249, <https://doi.org/10.1029/2018RG000615>, 2019.

698 Sadavarte, P. and Venkataraman, C.: Trends in multi-pollutant emissions from a technology-linked
699 inventory for India: I. Industry and transport sectors, *Atmospheric Environment*, 99, 353–364,
700 <https://doi.org/10.1016/j.atmosenv.2014.09.081>, 2014.

701 Satheesh, S. K.: *Letter to the Editor*
702 Aerosol radiative forcing over land: effect of surface and
702 <https://doi.org/10.5194/angeo-20-2105-2002>, 2002.

703 Shalaby, A., Zakey, A. S., Tawfik, A. B., Solmon, F., Giorgi, F., Stordal, F., Sillman, S., Zaveri, R. A., and
704 Steiner, A. L.: Implementation and evaluation of online gas-phase chemistry within a regional climate
705 model (RegCM-CHEM4), 5, 741–760, <https://doi.org/10.5194/GMD-5-741-2012>, 2012.

706 Singh, A., Rastogi, N., Kumar, V., Slowik, J. G., Satish, R., Lalchandani, V., Thamban, N. M., Rai, P.,
707 Bhattu, D., Vats, P., Ganguly, D., Tripathi, S. N., and Prévôt, A. S. H.: Sources and characteristics of
708 light-absorbing fine particulates over Delhi through the synergy of real-time optical and chemical
709 measurements, *Atmospheric Environment*, 252, 118338,
710 <https://doi.org/10.1016/j.atmosenv.2021.118338>, 2021.

711 Solmon, F., Giorgi, F., and Liousse, C.: Aerosol modelling for regional climate studies: Application to
712 anthropogenic particles and evaluation over a European/African domain, 58, 51–72,
713 <https://doi.org/10.1111/j.1600-0889.2005.00155.x>, 2006.

714 Srivastava, A. K., Dey, S., and Tripathi, S. N.: Aerosol Characteristics over the Indo-Gangetic Basin:
715 Implications to Regional Climate, IntechOpen, <https://doi.org/10.5772/47782>, 2012.

716 Su, W., Charlock, T. P., and Rose, F. G.: Deriving surface ultraviolet radiation from CERES surface and
717 atmospheric radiation budget: Methodology, 110, <https://doi.org/10.1029/2005JD005794>, 2005.

718 Tibrewal, K. and Venkataraman, C.: Climate co-benefits of air quality and clean energy policy in India,
719 4, 305–313, <https://doi.org/10.1038/s41893-020-00666-3>, 2021.

720 Tiedtke, M.: Representation of Clouds in Large-Scale Models, 121, 3040–3061,
721 [https://doi.org/10.1175/1520-0493\(1993\)121<3040:ROCILS>2.0.CO;2](https://doi.org/10.1175/1520-0493(1993)121<3040:ROCILS>2.0.CO;2), 1993.

722 Tripathi, S. N., Dey, S., Tare, V., Satheesh, S. K., Lal, S., and Venkataramani, S.: Enhanced layer of
723 black carbon in a north Indian industrial city, 32, <https://doi.org/10.1029/2005GL022564>, 2005.

724 Venkataraman, C.: Supplement of Source influence on emission pathways and ambient PM 2.5
725 pollution over India (2015–2050) The copyright of individual parts of the supplement might differ
726 from the CC BY 4.0 License, 18, 8017–8039, <https://doi.org/10.5194/acp-18-8017-2018-supplement>,
727 2018.

728 Venkataraman, C., Brauer, M., Tibrewal, K., Sadavarte, P., Ma, Q., Cohen, A., Chaliyakunnel, S.,
729 Frostad, J., Klimont, Z., Martin, R. V., Millet, D. B., Philip, S., Walker, K., and Wang, S.: Source
730 influence on emission pathways and ambient PM2.5 pollution over India (2015–2050), 18, 8017–
731 8039, <https://doi.org/10.5194/acp-18-8017-2018>, 2018.

732 Venkataraman, C., Bhushan, M., Dey, S., Ganguly, D., Gupta, T., Habib, G., Kesarkar, A., Phuleria, H.,
733 and Sunder Raman, R.: Indian network project on carbonaceous aerosol emissions, source
734 apportionment and climate impacts (COALESCE), 101, E1052–E1068, <https://doi.org/10.1175/BAMS-D-19-0030.1>, 2020.

736 Zakey, A. S., Solmon, F., and Giorgi, F.: Implementation and testing of a desert dust module in a
737 regional climate model, *Atmos. Chem. Phys.*, 2006.

738 Zakey, A. S., Giorgi, F., and Bi, X.: Modeling of sea salt in a regional climate model: Fluxes and
739 radiative forcing, 113, 14221, <https://doi.org/10.1029/2007JD009209>, 2008.

740